Dopant solubility in ceria: alloy thermodynamics combined with the DFT+U calculations

David Fuks[a], Denis Gryaznov[b], Eugene Kotomin[b,c,d], Andrew Chesnokov[b], Joachim Maier[c]

[a] Department of Materials Engineering, Ben Gurion University of the Negev, Beer Sheva 84105, Israel

[b] Institute of Solid State Physics, University of Latvia, Kengaraga 8, Riga LV-1063, Latvia

[c] Max Planck Institute for Solid State Research, Heisenbergstr. 1, Stuttgart D-70569, Germany

[d] Photochemistry Center, Russian Academy of Sciences, Moscow, 119421 Russia

Abstract. Tb-doped CeO_2 (ceria) is a promising mixed conductor for oxygen permeation membranes and reversible oxygen sorbents. To predict solubility of Tb ions in ceria for a wide range of concentrations, density functional theory (DFT+U) calculations with two different values of Hubbard U-parameter on Tb and Ce ions were combined with alloy thermodynamics and the Concentration Wave approach. It is shown that, to predict properties of disordered solid solutions at finite temperatures, the energy parameters in the mixing energies can be extracted from the DFT+U calculations performed at T=0 K for two ordered configurations of the dopant in the supercells. The unlimited solubility of Tb^{4+} in CeO_2 in the quasi-binary cross-section CeO_2-TbO_2 is predicted in the temperature range where both stoichiometric TbO_2 and CeO_2 reveal fluoride structures (above 700^{o}C).

Keywords: CeO_2, Tb, solid solution, solubility, ab initio, thermodynamics

1. Introduction

CeO_2 (ceria) exhibits a fluorite structure with Ce^{4+} ions being 8-fold coordinated with O^{2-} ions. Doped ceria can be used in numerous applications, including electrolytes of solid oxide fuel cells [1], membranes for oxygen separation [2], oxygen sensors [3], catalysis [4], micro-electro-mechanics ([5] and references therein). Trivalent rare earth dopants, e.g. Gd^{3+}, Sm^{3+}, and Pr^{3+} promote oxygen vacancy

formation and thus enable ionic conductivity [6,7]. Unlike Gd and Sm, Pr and Tb ions can be in either 3+ or 4+ oxidation state. Ceria doped with Tb is a prospective material for mixed-conductive membranes for oxygen separation [2,8]. It is attractive due to a combination of fast transport of oxygen ions, favorable redox catalytic properties and pronounced chemical compatibility with water and carbon dioxide at high temperatures. Ceria-based membranes offer competitive oxygen permeation fluxes at temperatures below 1123 K as compared with perovskite-based membranes [9,10]. Special attention has been paid to doping with lanthanide oxides, which are soluble in ceria up to ~40% [11].

In the $Ce_{1-c}Tb_cO_{2-\delta}$ system, the structure properties with respect to transport were discussed in detail [12], while in the accompanying study [13] different compositions of $Ce_{1-c}Tb_cO_{2-\delta}$ (x =0.1, 0.2, 0.5), either undoped or cobalt-doped, have been prepared and characterized, to assess its applicability as the oxygen separation membranes. To gain insight into the transport properties of terbium-doped ceria, several bulk-related properties were investigated, using X-ray diffraction (XRD), temperature-programmed desorption (TPD), thermogravimetry (TG), DC-conductivity and UV-vis spectrophotometry. Analysis of the Vegard's law indicates that the lattice parameter indeed follows a linear concentration trend indicating absence of secondary phases in these solid solutions. In agreement with these experimental observations, the Tb impurities in CeO_2 are in a mixed valence state. The actual proportion of Tb^{3+} and Tb^{4+} ions in CeO_2 lattice depends on experimental conditions, i.e. temperature and oxygen partial pressure. In the present study, we demonstrate that Tb^{4+} ions are completely soluble in ceria at any concentrations.

Phase diagrams of $Ce_{1-c}Gd_cO_{2-c/2}$ were recently calculated [14,15]. It was shown that the phase separation into Gd_2O_3 and CeO_2 occurs below certain transition temperature that weakly depends on the Gd concentration. At the same time, to the best of our knowledge, there is no information about the solubility of Tb in CeO_2 in the whole range of atomic fractions of Tb. Experiments on solid solutions with Tb content up to 60% [13] do not indicate second phase formation. On the other hand, the EELS and TEM measurements [16] demonstrated the formation of domains containing Tb^{3+} and oxygen vacancies, in the range of Tb concentration from 0 to 50% with a secondary phase formation observed in XRD for Tb concentrations higher than 80% [17]. They also show oxygen vacancy ordering in domains with trivalent dopants in Sm, Gd, Dy, and Yb-doped CeO_2 [18]. The oxygen vacancy ordering effect explains anomalies in

the behavior of the lattice constant in Pr-doped CeO_2 thin films [19]. Thus, understanding solubility data may be important for the use of $Ce_{1-c}Tb_cO_2$ for oxygen separation, because, as was observed in ref. [20], the increase in Tb content leads to an increase in the oxygen uptake.

The aim of this paper is to calculate solubility of Tb^{4+} in ceria in a whole range of dopant concentrations.

2. Computational methods and basic properties of $Ce_{0.5}Tb_{0.5}O_2$

CeO_2 crystallizes in the fluorite structure (space group $Fm\bar{3}m$, face-centered cubic lattice) with a primitive unit cell of three atoms, and the angle of 60º between the lattice vectors. Its conventional unit cell has 12 atoms with an angle of 90º between the lattice vectors which probably is one of reasons, why it is so widely used in DFT calculations. In the present study, we used two supercells to calculate two superstructures for the concentration of Tb impurity in CeO_2 fixed at 50%, which is necessary for the further thermodynamic analysis (Section 3). Tb ion substitutes for Ce in the cation fcc sub-lattice of the fluorite structure. We built two supercells for two different distributions of Tb impurity (hereafter, superstructures **1** and **2**). Namely, the first supercell represented a layered Tb impurity arrangement in the [001] direction of the conventional unit cell (the tetragonal space group P4/mmm) and, consequently, consisted of 12 atoms (fig. 1a). The other one was generated by the 2x2x2 transformation matrix for the lattice translational vectors of the primitive unit cell. The layered Tb-impurity arrangement in the [111] direction (the rhombohedral space group $R\bar{3}m$) was used for the superstructure **2** and, therefore, consisted of 24 atoms (fig. 1b).

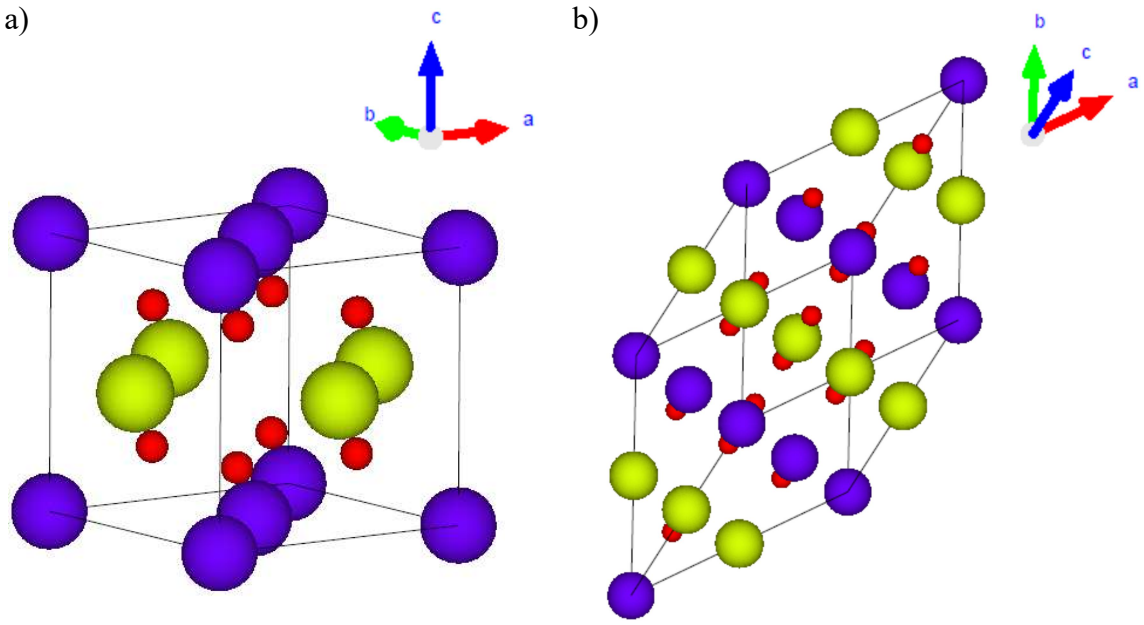

Fig. 1. Two superstructures of $Ce_{0.5}Tb_{0.5}O_2$ corresponding to a) $\vec{k}_1 = \frac{2\pi}{a}(0,0,1)$ and (b) $\vec{k}_2 = \frac{2\pi}{a}\left(\frac{1}{2},\frac{1}{2},\frac{1}{2}\right)$, considered in the calculations. Yellow, blue and red balls represent Ce, Tb and O atoms, respectively.

We used the VASP 5.4 code [21,22] with the projected augmented wave method [23] and the scalar relativistic pseudopotentials substituted for 46 electrons on Tb and Ce and 2 electrons on O atoms. The exchange-correlational functional was that due to Perdew, Becke and Ernzerhof (PBE) [24]. We employed the rotationally-invariant Dudarev's form of the so-called PBE+U_{eff} approach [25] as implemented in the VASP code. The two values of the Hubbard U_{eff}-parameter (hereafter, U) were fixed separately on 4f-orbitals of Ce and Tb atoms, their magnitudes selected according to the literature data, i.e. 5.0 eV [26,27] and 6.0 eV [28], respectively. The cut-off energy was fixed at 520 eV throughout all the spin-polarized (ferro-magnetic) calculations with the full atomic and electronic structure optimization. The lattice parameters and internal coordinates were optimized until the energy difference became less than 10^{-6} eV. The integration in the reciprocal space over the Brillouin zone was performed using the Γ-centered 4x4x4 *k*-point mesh for the conventional unit cell (perfect CeO_2 and TbO_2, superstructure **1**) and 3x3x3 *k*-point mesh for the superstructure **2**. Effective atomic charges and magnetic moments were calculated using topological Bader analysis [29,30].

As known, TbO_2 (the limiting case of $Ce_{1-c}Tb_cO_2$ for c=1) could be non-stoichiometric on oxygen sub-lattice which leads to symmetry reduction and, very much likely, two types of Tb ions, in both oxidation states 3+ and 4+ [31,32]. We do not consider non-stoichiometric TbO_2 in the present study, focusing on the oxidation state 4+ used in our thermodynamic analysis. Note that the fluorite structure of TbO_2 was considered in the experimental studies [12,17]. Therefore, in the present study, stoichiometric TbO_2 was also calculated in the fluorite structure.

We put emphasis on the analysis of the density of states (DOS) of $Ce_{0.5}Tb_{0.5}O_2$ and of the parent compounds which should show the main features with respect to cations in the oxidation state 4+. In pure CeO_2 the valence band (corresponding to O^{2-} ions) consists mainly of O *2p* states whereas the empty Ce *4f* band (corresponding to Ce 4+ oxidation state) lies between the valence band and bottom band formed by Ce *5d* states (Fig. 2). The two band gap values are given in Table 1. It has been shown in the literature that the DFT+U approach or, alternatively, calculations involving hybrid density functional, are necessary to correctly reproduce the band gap in CeO_2.

In our calculations of TbO_2 and CeO_2 the PBE+U approach slightly underestimated the experimental band gaps (Table 1). The importance of including strong correlation effects for TbO_2 was already demonstrated in an earlier study [28]. Note the considerable difference for DOS in TbO_2 and CeO_2. Indeed, the valence band in TbO_2 is formed by O *2p* electrons hybridized with Tb *4f* spin down electrons at ca. -2 eV below the Fermi energy (Fig. 2). The Fermi energy is crossing the valence band in the spin down channel which could hint on a *p*-type conductivity in a stoichiometric TbO_2. Its band gap (2.8 eV, Table 1) was estimated between the top of valence band (O*2p* electrons) and empty Tb *4f* band. This empty Tb*4f* band lies much closer to the bottom of conduction band, formed by Tb *5d* states, as compared to the CeO_2 (the gap between the Ce *4f* empty band and Ce *5d* states ~2.0 eV). There is also a sharp Tb *4f* peak in the spin up electrons at ~6.3 eV below the Fermi energy.

As expected, the DOS of $Ce_{0.5}Tb_{0.5}O_2$ in Fig.3 shows main characteristics of the two parent compounds. The empty Tb *4f* band lies above the empty Ce *4f* band. Thus, there is an additional band gap (O *2p* – Tb *4f*) in comparison with CeO_2 (Table 1). This is why there are two main differences between the two parent compounds and $Ce_{0.5}Tb_{0.5}O_2$. First, the band gap between the O *2p* band and cation *5d* empty states (both cations

equally contribute to the conduction band bottom in $Ce_{0.5}Tb_{0.5}O_2$) is larger in the superstructures than in a pure TbO_2, i.e. 4.2 eV vs 3.1 eV. Second, the band gap between the O *2p* band and Ce *4f* empty states is smaller in the superstructures than in CeO_2, i.e. 1.3(1.2) eV vs 2.1 eV. As for pure TbO_2, we observe the *p*-type conductivity in $Ce_{0.5}Tb_{0.5}O_2$ (Fig. 3), in agreement with the experimental observations ([12,13] and references therein).

It should be emphasized that Tb^{4+} has the magnetic moment (effective charge) of 6.22 μ_B (2.17 e) - 6.23 μ_B (2.18 e) in both superstructures, and a similar value of 6.20 μ_B (2.18 e) in TbO_2 corresponding to the high spin state (formally 7 μ_B). The effective atomic charges of Tb and Ce cations do not change significantly in the superstructures, in comparison with CeO_2. The lattice constant of 12 atom unit cell is unchanged in the superstructure **1**. The lattice constant of CeO_2 and the superstructure **1** is larger than that the experimental one (Table 1) which is typical for DFT+U formalism.

Table 1. Lattice parameters (*a*), band gap (ΔE_g), Bader effective charges (q) and magnetic moment (μ) of Tb for CeO_2, TbO_2 and the superstructures. Experimental values from the literature are given in parentheses. The conventional unit cell was used for perfect CeO_2 and TbO_2. Me denotes both Ce and Tb cations contributing to the conduction band bottom.

	CeO_2 ($Fm\bar{3}m$)	Superstructure 1 (P4/mmm)	Superstructure 2 ($R\bar{3}m$)	TbO_2 ($Fm\bar{3}m$)
a / Å	5.50 (5.41[a])	5.51 / 5.29	7.67 / 60.22°	5.35 (5.22[b], 5.31[c])
ΔE_g / eV	O 2p – Ce 4f: 2.1 (~ 3[d]) O 2p – Ce 5d: 5.2 (~6[d])	O 2p – Ce 4f: 1.3 O 2p – Tb 4f: 3.2 O 2p – Me 5d: 4.2	O 2p – Ce 4f: 1.2 Ce 4f – Tb 4f: 3.1 O 2p – Me 5d: 4.2	O 2p – Tb 4f: 2.8 O 2p – Tb 5d: 3.1
q / e	Ce: 2.34	Tb: 2.18 Ce: 2.35	Tb: 2.17 Ce: 2.38	Tb: 2.18
μ / μ_B	—	Tb: 6.23	Tb: 6.22	Tb: 6.20

[a] ref. [33] , [b] ref.[31], [c] ref.[34], [d] ref.[35]

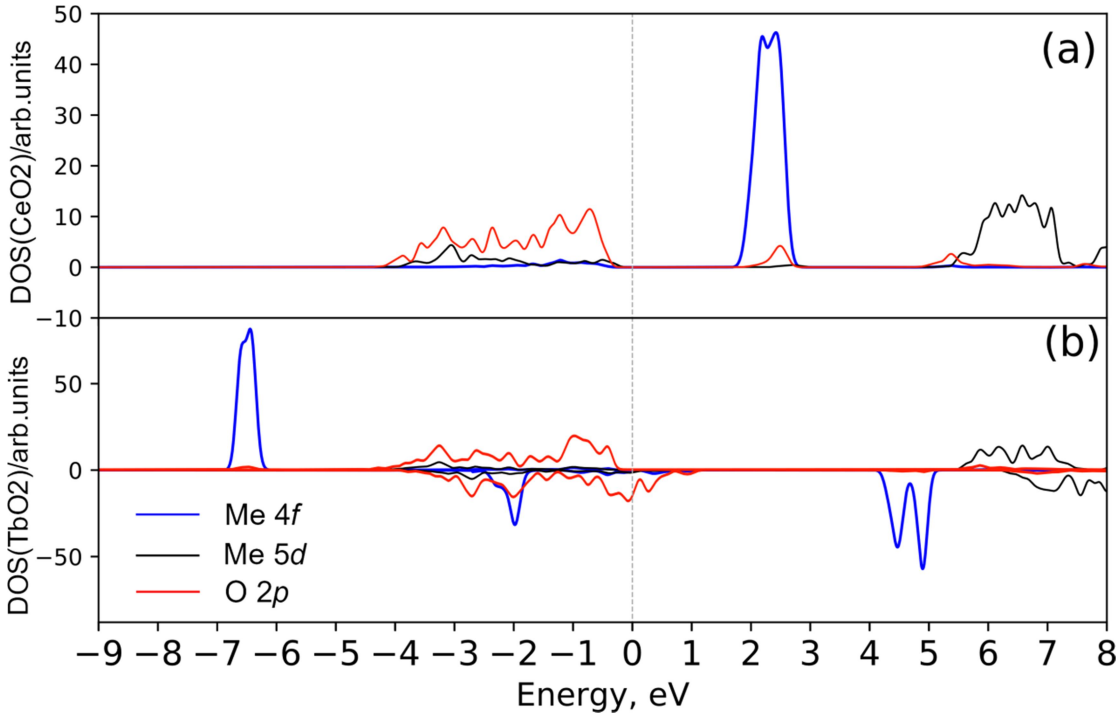

Fig. 2. The **projected density of states** (DOS) for CeO_2 (a) and TbO_2 (b). The Fermi energy is set to zero. The DOS for spin down electrons in a) is similar to that for spin up and is not shown. Me stands for Ce (a) and Tb (b) cation *5d* states, respectively. In b) Tb *4f* peak at ~ -2 eV was multiplied for better visibility by the factor of 4.

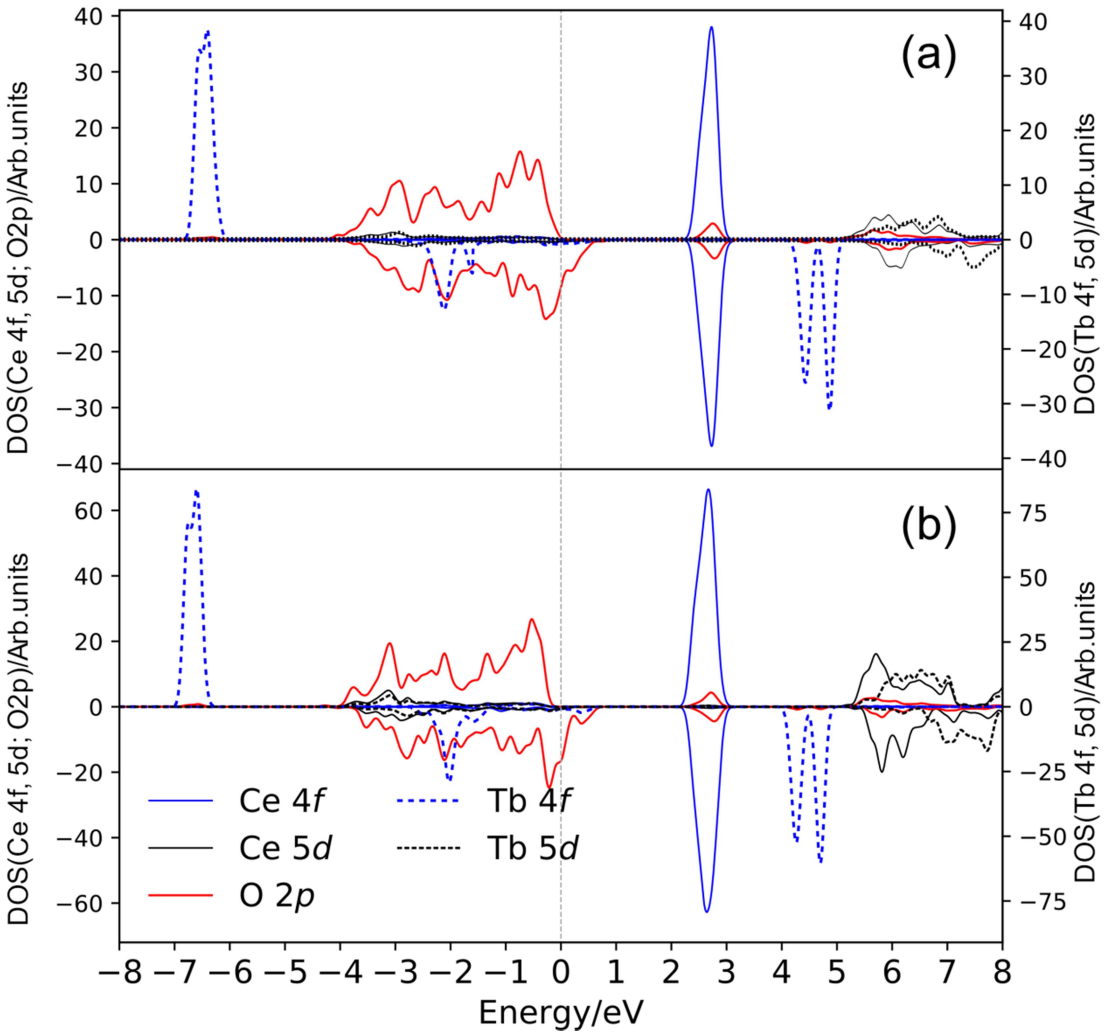

Fig. 3. Projected DOS for superstructure **1** (a) and superstructure **2** (b). The Fermi energy is set to zero. The Tb *4f* peak at ~ -2 eV was multiplied for better visibility by the factor of 4.

3. Thermodynamic Analysis of solubility of Tb in CeO_2

3.1.Main approach

We combined DFT with the statistical thermodynamic approach for modeling the formation of $(Ce_{1-c}Tb_c)O_2$ solid solutions, with the aim to predict solubility limits of Tb^{4+} in ceria. It should be noted that the supercell model used in our DFT+U calculations is applicable only for absolutely ordered structures. To investigate the behavior of the system at finite temperatures from such calculations of the ordered phases at T=0 K, it is necessary to formulate the problem in a way that allows us to extract the energy parameters for further thermodynamic analysis

of the relative stability of the structures beyond T=0 K. These parameters may be used for studying disordered or partly ordered solid solutions. The DFT calculations have been widely applied in the study of alloy phase stability and the calculation of composition-temperature phase diagrams [36–39]. Several statistical thermodynamics methods may be linked with the DFT calculations results for the analysis of the relative stability of phases at T≠0K. Among them are lattice Monte Carlo (MC) approach, Cluster expansion method (CE) (see for example Refs [14,39–41], and Concentration Waves method (CW). In our study the latter approach, as formulated in ref. [42] was used. It has several advantages over other statistical theories of alloys. One such advantage is that the distribution of B atoms in a binary A–B alloy is described by a single occupation probability function, $n(\vec{R})$. This function gives the probability to find the atom B (Tb, in our case) at the site $\vec{R}$ of the lattice. Such approach was successfully used previously to analyze the initial stages of the growth of thin metallic films on the ceramic substrate [43–46], to explain the behavior of complex perovskites [47–50], and for description of the phase competition and solubility of doping elements in some thermoelectric compounds [51–53]. It is based on the treatment of the ordering phases in the crystalline structure of solid solution which are stable with respect to the formation of antiphase domains. The choice of these ordered structures does not depend on the type of interatomic interactions and is dictated only by symmetry considerations [54,55].

We consider $(Ce_{1-c}Tb_c)O_2$ solid solutions with a varied fraction of Tb atoms in the fluorite structure where Ce or Tb atoms occupy the sites of *fcc* lattice immersed in the field of the rest oxygen atoms that form the background lattice. Varying the Tb concentration c in the analysis of the phase stability of *fcc* sub-lattice is equivalent considering the quasi-binary cross-section of the ternary Ce-Tb-O phase diagram. Thermodynamics of such solid solutions may be formulated as in Ref. [42], in terms of the effective interatomic mixing potential in A-B alloys that are $(Ce_{1-c}Tb_c)$ in our case. The variation of the atomic fraction of Tb changes the interaction of the Ce-Tb sub-system with the oxygen background, which in its turn changes also Ce-Ce, Ce-Tb, and Tb-Tb interactions, meaning that the latter differ from these in binary Ce-Tb solid solutions. This is automatically accounted for in the DFT calculations (or, DFT+U calculations in our case) because of their self-consistent character.

The effective interatomic mixing potential is expressed in the form

$$\tilde{V}(\vec{R},\vec{R}') = V_{CeCe}(\vec{R},\vec{R}') + V_{TbTb}(\vec{R},\vec{R}') - 2V_{CeTb}(\vec{R},\vec{R}'), \quad (1)$$

where $V_{CeCe}(\vec{R},\vec{R}'), V_{TbTb}(\vec{R},\vec{R}')$ and $V_{CeTb}(\vec{R},\vec{R}')$ are the effective interatomic potentials between Ce-Ce, Tb-Tb and Ce-Tb pairs. $\vec{R}$ and $\vec{R}'$ are the sites in the *fcc* sub-lattice. The configurational part of the free energy for a solid solution (neglecting the phonon contribution) in CW approach is given by [42]:

$$F = \frac{1}{2}\sum_{\substack{\vec{R},\vec{R}',\\ \vec{R}\neq\vec{R}'}} \tilde{V}(\vec{R},\vec{R}')\, n(\vec{R})\, n(\vec{R}') +$$

$$kT\sum_{\vec{R}}[n(\vec{R})\ln\left(n(\vec{R})\right) + (1-n(\vec{R}))\ln(1-\left(n(\vec{R})\right))] - \mu\sum_{\vec{R}} n(\vec{R})\,. \quad (2)$$

Summation in Eq. (2) runs over the sites of the Ising lattice (*fcc* in our case) with Ce and Tb atoms distributed in it. The first term in Eq. (2) corresponds to the internal energy, the second one the entropy term (−TS), and μ the indefinite multiplier of Lagrange, playing the role of the chemical potential. The function $n(\vec{R})$ that determines the distribution of solute atoms in the ordered superstructures that are stable with respect to the formation of antiphase domains may be expanded into the Fourier series

$$n(\vec{R}) = c + \tfrac{1}{2}\textstyle\sum_s \eta_s \sum_{j_s}[\gamma_s(j_s)\exp(i\vec{k}_{j_s}\vec{R}) + \gamma_s^*\exp(-i\vec{k}_{j_s}\vec{R})]\,, \quad (3)$$

where $\vec{k}_{j_s}$ are the vectors of the reciprocal lattice belonging to the star s, j_s numerates the vectors of the star s, and $\gamma_s(j_s)$ are coefficients that determine the symmetry of the function $n(\vec{R})$ with respect to reflection and rotation operations. $n(\vec{R})$ linearly depends on the long range order (LRO) parameters, η_s, of the superstructures that may be formed on the basis of the Ising lattice of the disordered solid solution. The LRO parameters are defined in such a way that they are equal to unity in a completely ordered state, where the occupation probabilities $n(\vec{R})$ on all the lattice sites $\{\vec{R}\}$ are either unity or zero. For the disordered state all η_s are equal to zero. Substitution of Eq. (3) into (2) allows to present the free energy of formation of solid solution in terms of Fourier transforms of the effective interatomic mixing potential, $\tilde{V}(\vec{k}_{j_s})$.

$$\tilde{V}(\vec{k}_{j_s}) = \textstyle\sum_i \tilde{V}(\vec{R}_i)\cdot\exp(i\vec{k}_{j_s}\vec{R}_i) \quad (4)$$

To determine the single-valued LRO parameters an additional normalization condition for $\gamma_s(j_s)$ should be used, viz.

$$\textstyle\sum_{j_s}\gamma_s(j_s) = 1 \quad (5)$$

In the study of solubility trends in $(Ce_{1-c}Tb_c)O_2$ two absolutely ordered superstructures presented in Fig. 1 are considered. These superstructures are determined by the vectors $\vec{k}_1 = \frac{2\pi}{a}(0,0,1)$ and $\vec{k}_2 = \frac{2\pi}{a}\left(\frac{1}{2},\frac{1}{2},\frac{1}{2}\right)$ with 'a' being the cubic lattice parameter. Substituting these vectors $\vec{k}_1$ or $\vec{k}_2$ in Eq.(3) gives the corresponding occupation probabilities $n(\vec{R})$ for these superstructures

$$n_1(\vec{R}) = c + \eta_1\gamma_1\exp(2\pi iz) \quad (6)$$

$$n_2(\vec{R}) = c + \eta_2\gamma_2\exp(i\pi(x+y+z)) \quad (7)$$

In stoichiometric composition for these structures for an absolutely ordered state the Tb concentration, *c* on the Ce-Tb sub-lattice is equal to 0.5 and LRO parameters are equal to unity, giving $\gamma_1 = \gamma_2 = 1/2$.

Substituting Eqs. (6,7) into Eq. (1), the free energies of formation for the superstructure 1 and 2 (per site of *fcc* sub-lattice), respectively, may be obtained as

$$\boldsymbol{F_1 = \frac{1}{2}\tilde{V}(0)c(c-1) + \frac{1}{8}\tilde{V}(\vec{k}_1)\eta_1^2 +}$$
$$\boldsymbol{kT\left[\left(c+\tfrac{1}{2}\eta_1\right)ln\left(c+\tfrac{1}{2}\eta_1\right) + \left(1-c-\tfrac{1}{2}\eta_1\right)\ln\left(1-c-\tfrac{1}{2}\eta_1\right)\right],} \quad (8)$$

$$\boldsymbol{F_2 = \frac{1}{2}\tilde{V}(0)c(c-1) + \frac{1}{8}\tilde{V}(\vec{k}_2)\eta_2^2 +}$$
$$\boldsymbol{kT\left[\left(c+\tfrac{1}{2}\eta_2\right)ln\left(c+\tfrac{1}{2}\eta_2\right) + \left(1-c-\tfrac{1}{2}\eta_2\right)\ln\left(1-c-\tfrac{1}{2}\eta_2\right)\right],} \quad (9)$$

where $\boldsymbol{\tilde{V}(0)}$ is the Fourier transform of the effective interatomic mixing potential for *k*=0. These free energies show the preference of the structures with respect to the standard state that is the mixture of constituents, CeO_2 and TbO_2, with the energy

$$\boldsymbol{E_{stand} = E_{CeO_2}\cdot(1-c) + E_{TbO_2}\cdot c,} \quad (10)$$

where E_{CeO_2} and E_{TbO_2} are the total energies of CeO_2 and TbO_2 calculated using DFT+U in the fluorite structure at T=0K, respectively. In Eqs. 8 and 9 the first two terms present the mixing energies for considered structures, and the last term is the configurational entropy of mixing. For absolutely ordered structures at stoichiometric compositions at T=0 K c_{st}=1/2 and $\eta_{1,2}$=1 the mixing energies have the form

$$\Delta E_1 = \frac{1}{8}\tilde{V}(0) + \frac{1}{8}\tilde{V}(\vec{k}_1) \quad (11)$$

$$\Delta E_2 = \frac{1}{8}\tilde{V}(0) + \frac{1}{8}\tilde{V}(\vec{k}_2) \quad (12)$$

and may be obtained from the DFT calculations as the differences between the total energies of corresponding superstructures and the total energy of the mixture of constituents given by Eq. 10. As follows from Eq. 4

$$\widetilde{V}(\vec{k}_1) = -4\widetilde{V}(\vec{R}_1) + 6\widetilde{V}(\vec{R}_2) - 8\widetilde{V}(\vec{R}_3) + \cdots, \quad (13)$$

$$\widetilde{V}(\vec{k}_2) = -6\widetilde{V}(\vec{R}_2) + 12\widetilde{V}(\vec{R}_4) + \cdots, \quad (14)$$

$$\widetilde{V}(0) = 12\widetilde{V}(\vec{R}_1) + 6\widetilde{V}(\vec{R}_2) + \cdots. \quad (15)$$

With the approximation of interactions in the two nearest neighbors on the Ce/Tb sub-lattice this gives

$$\Delta E_1 = \widetilde{V}(\vec{R}_1) + \tfrac{3}{2}\widetilde{V}(\vec{R}_2), \quad (16)$$

$$\Delta E_2 = \tfrac{3}{2}\widetilde{V}(\vec{R}_1). \quad (17)$$

3.2. Main results

The parameters ΔE_1 and ΔE_2 calculated for the superstructures 1 and 2 suggest $\Delta E_1 = 0.228$ eV and $\Delta E_2 = 0.056$ eV, respectively. Their positive sign means that both superstructures in Fig.1 are energetically unfavorable in comparison with the mixture of constituents, CeO_2 and TbO_2, and, in reality, do not exist. At the same time, the discussed procedure allows us to calculate the energy parameter $\widetilde{V}(0)$ that is responsible for the behavior of the *disordered* solid solution on Ce/Tb sub-lattice. Solving Eqs. (16,17), $\widetilde{V}(\vec{R}_1)$ and $\widetilde{V}(\vec{R}_2)$ were found, and after substitution into Eq. (15) it yields $\widetilde{V}(0)$ =1.210 eV. Let us compare Eqs. (8,9) for absolutely disordered structures (η_1=0, η_2=0) with the model of regular solid solution frequently used for construction of phase diagrams [56]. In this model, the free energy of mixing for the disordered solid solution is presented as $\Delta F_{mix}=\Delta E-T\Delta S$, with ΔE standing for the mixing energy could be written in the form $\Delta E=L\cdot c\cdot(1-c)$ and ΔS is the configuration entropy of mixing. It is easy to find that $L= -\frac{1}{2}\widetilde{V}(0)$.

This consideration demonstrates that the DFT+U calculations of the formation energies for only two $(Ce_{0.5}Tb_{0.5})O_2$ *absolutely ordered* structures allows obtaining the energy parameter that determines the mixing energy for *disordered* $(Ce_{1-c}Tb_c)O_2$ solid solution. With this data in hand the free energy of mixing may be calculated, and the solubility trends at different temperatures and concentrations, *c,* may be found. It should be mentioned that, as demonstrated in ref. [15], the Cluster Interaction parameters, V_{AA}, V_{BB}, and V_{AB} applied in the CE

method to study the decomposition in $Ce_{1-c}Gd_cO_{2-c/2}$ solid solutions, do not depend on the dopant concentration. Based on this result, it is reasonable to assume that $\tilde{V}(0)$ determined by Eq. (1) and Eq. (4) (for $\vec{k}_s$=0) is also concentration independent and, thus, we can use the above expression for mixing energy with L=*const* in the whole concentration range.

In Fig. 4 the concentration dependence of the mixing energy, configuration entropy of mixing term, (-*TΔS*), and the free energy of mixing, are presented (per formula unit, f.u.), as an example, for T=1000 K.

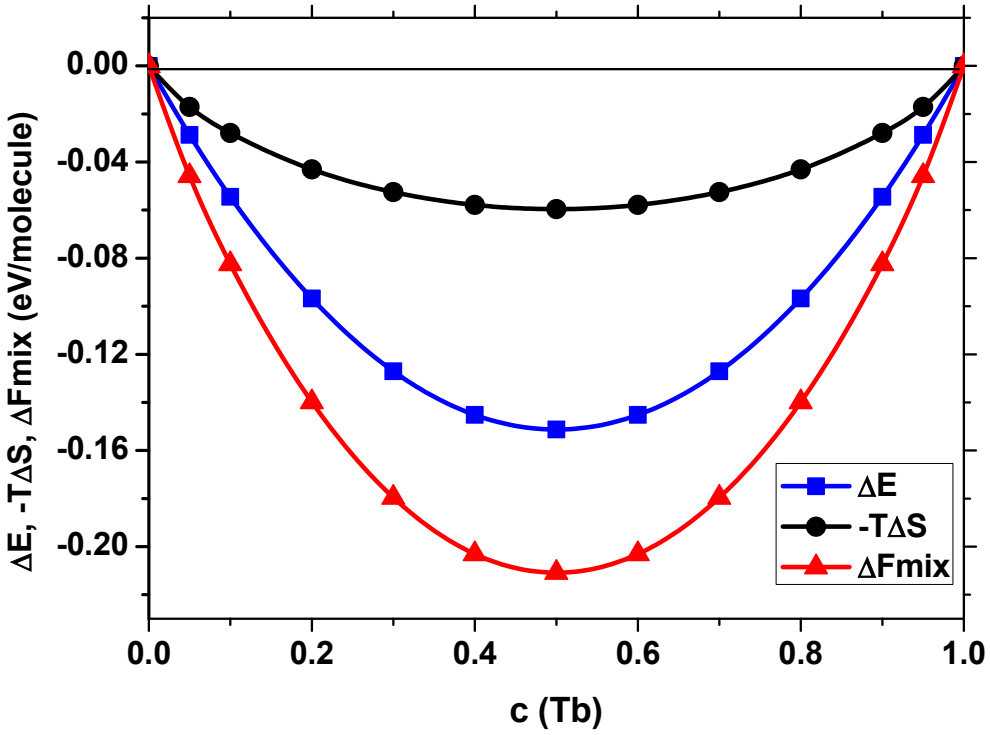

Fig. 4. Tb^{4+} ion concentration dependence of the mixing energy ΔE, configuration entropy of mixing term, (-*TΔS*), and the free energy of mixing ΔF_{mix} for T=1000 K when both parent compound exhibit fluorite structure.

It may be seen that ΔF_{mix} is concave in the whole concentration range with no inflection points. Thus, an unlimited solubility of Tb in CeO_2 in the quasi-binary cross-section CeO_2-TbO_2 should be observed in the temperature range where TbO_2 and CeO_2 fluoride structures exist. As follows from the binary Tb-O and Ce-O phase diagrams, this temperature region is above ~700°C [57,58].

4. Conclusions

Combined analysis of alloy thermodynamics and DFT+U calculations of ordered dopant structures allows us to predict unlimited solubility of the Tb^{4+} ions in ceria above 1000 K (in contrast to Gd). Note that our approach has several disadvantages as compared e.g. with cluster variation method (see, for example,[59,60]). First, it is based on mean-field approximation that fails in prediction of correct temperatures of order-disorder phase transformations. However, in our case, the considered structures are shown to be unfavorable with respect to decomposition, and, thus, there is no need to discuss their disordering when the temperature increases. The obtained mixing energies for these structures are used only for the estimation of the mixing parameter in the *disordered* solid solution which is energetically preferable. Second, the considered entropy term does not account for the correlations in the disordered system, to specify the state of clustering or short-range order in an alloy [61]. However, keeping in mind the fact that the entropy term adds a negative contribution to the free energy of mixing, the peculiarities of the entropy of mixing are not important: since for disordered solid solution $(Ce_{1-c}Tb_c)O_2$ $\Delta E<0$ in a whole concentration range, the correlations cannot change the predicted trend - unlimited solubility of Tb in CeO_2. Finally, as mentioned above, we consider the model of regular solid solutions, but more complicated models like sub-regular solid solution model may be important, if the limited solubility would be obtained. This will result in non-symmetric (with respect to c=0.5) solubility limits in the system (e.g. [62]). This is again not our case. At the same time, the applied approach allows prediction of the solubility or decomposition tendencies in a very simple way that avoids long time-consuming calculations. Summing up, our simple method could be used for many systems where filtering of the solubility tendencies is desirable before the detailed study of phase transformations.

Acknowledgments. This research was partly funded by the Russian Science Foundation (under the project 14-43-0005) and ERA-NET HarvEnPiez project, with the computer resources provided by Stuttgart Supercomputing Centre (Project DEFTD 12939). A. C. also acknowledges financial support from the University of Latvia Foundation (Arnis Riekstins's ''MikroTik'' donation). Authors thank R. Merkle, A. Popov for fruitful discussions.

References

[1] J.M. Serra, V.B. Vert, M. Betz, V.A.C. Haanappel, W.A. Meulenberg, F. Tietz, Screening of A-Substitution in the System A0.68Sr0.3Fe0.8Co0.2O3 − δ for SOFC Cathodes, J. Electrochem. Soc. 155 (2008) B207–B214. doi:10.1149/1.2818766.

[2] J. Sunarso, S. Baumann, J.M. Serra, W.A. Meulenberg, S. Liu, Y.S. Lin, J.C. Diniz da Costa, Mixed ionic–electronic conducting (MIEC) ceramic-based membranes for oxygen separation, J. Memb. Sci. 320 (2008) 13–41. doi:10.1016/j.memsci.2008.03.074.

[3] P. Jasinski, T. Suzuki, H.U. Anderson, Nanocrystalline undoped ceria oxygen sensor, Sens. Actuators B Chem. 95 (2003) 73–77. doi:10.1016/S0925-4005(03)00407-6.

[4] W.C. Chueh, C. Falter, M. Abbott, D. Scipio, P. Furler, S.M. Haile, A. Steinfeld, High-Flux Solar-Driven Thermochemical Dissociation of CO_2 and H_2O Using Nonstoichiometric Ceria, Science. 330 (2010) 1797. doi:10.1126/science.1197834.

[5] N. Yavo, O. Yeheskel, E. Wachtel, D. Ehre, A.I. Frenkel, I. Lubomirsky, Relaxation and saturation of electrostriction in 10 mol% Gd-doped ceria ceramics, Acta Mater. 144 (2018) 411–418. doi:10.1016/j.actamat.2017.10.056.

[6] S.R. Bishop, T.S. Stefanik, H.L. Tuller, Electrical conductivity and defect equilibria of Pr0.1Ce0.9O2-[small delta], Phys. Chem. Chem. Phys. 13 (2011) 10165–10173. doi:10.1039/C0CP02920C.

[7] H. Yahiro, K. Eguchi, H. Arai, Electrical properties and reducibilities of ceria-rare earth oxide systems and their application to solid oxide fuel cell, Solid State Ion. 36 (1989) 71–75. doi:10.1016/0167-2738(89)90061-1.

[8] H.J. Park, G.M. Choi, Oxygen permeability of gadolinium-doped ceria at high temperature, J. Eur. Ceram. Soc. 24 (2004) 1313–1317. doi:10.1016/S0955-2219(03)00555-7.

[9] M.P. Lobera, J.M. Serra, S.P. Foghmoes, M. Søgaard, A. Kaiser, On the use of supported ceria membranes for oxyfuel process/syngas production, J. Memb. Sci. 385–386 (2011) 154–161. doi:10.1016/j.memsci.2011.09.031.

[10] Luo Huixia, Efimov Konstantin, Jiang Heqing, Feldhoff Armin, Wang Haihui, Caro Jürgen, CO2-Stable and Cobalt-Free Dual-Phase Membrane for Oxygen Separation, Angew. Chem. Int. Ed. 50 (2010) 759–763. doi:10.1002/anie.201003723.

[11] V.V. Kharton, F.M. Figueiredo, L. Navarro, E.N. Naumovich, A.V. Kovalevsky, A.A. Yaremchenko, A.P. Viskup, A. Carneiro, F.M.B. Marques, J.R. Frade, Ceria-based materials for solid oxide fuel cells, J. Mater. Sci. 36 (2001) 1105–1117. doi:10.1023/A:1004817506146.

[12] M. Balaguer, C. Solís, J.M. Serra, Structural–Transport Properties Relationships on Ce1–xLnxO2−δ System (Ln = Gd, La, Tb, Pr, Eu, Er, Yb, Nd) and Effect of Cobalt Addition, J. Phys. Chem. C. 116 (2012) 7975–7982. doi:10.1021/jp211594d.

[13] M. Balaguer, C.-Y. Yoo, H.J.M. Bouwmeester, J.M. Serra, Bulk transport and oxygen surface exchange of the mixed ionic-electronic conductor Ce1-xTbxO2-[small delta] (x = 0.1, 0.2, 0.5), J. Mater. Chem. A. 1 (2013) 10234–10242. doi:10.1039/C3TA11610G.

[14] P.A. Žguns, A.V. Ruban, N.V. Skorodumova, Ordering and phase separation in Gd-doped ceria: a combined DFT, cluster expansion and Monte Carlo study, Phys. Chem. Chem. Phys. 19 (2017) 26606–26620. doi:10.1039/C7CP04106C.

[15] P.A. Žguns, A.V. Ruban, N.V. Skorodumova, Phase diagram and oxygen-vacancy ordering in the CeO2-Gd2O3 system: a theoretical study, Phys. Chem. Chem. Phys. 20 (2018) 11805–11818. doi:10.1039/C8CP01029C.

[16] F. Ye, T. Mori, D.R. Ou, J. Zou, G. Auchterlonie, J. Drennan, Compositional and valent state inhomogeneities and ordering of oxygen vacancies in terbium-doped ceria, J. Appl. Phys. 101 (2007) 113528. doi:10.1063/1.2738409.

[17] F. Ye, T. Mori, D.R. Ou, M. Takahashi, J. Zou, J. Drennan, Compositional dependence of electrical conductivity of Ce1−xTbxO2−δ (0⩽x⩽1), Renew. Energy. 33 (2008) 331–335. doi:10.1016/j.renene.2007.05.014.

[18] D.R. Ou, T. Mori, F. Ye, J. Zou, G. Auchterlonie, J. Drennan, Oxygen-vacancy ordering in lanthanide-doped ceria: Dopant-type dependence and structure model, Phys. Rev. B. 77 (2008) 024108. doi:10.1103/PhysRevB.77.024108.

[19] Y. Kuru, D. Marrocchelli, S.R. Bishop, D. Chen, B. Yildiz, H.L. Tuller, Anomalous Chemical Expansion Behavior of Pr0.2Ce0.8O2-δ Thin Films Grown by Pulsed Laser Deposition, J. Electrochem. Soc. 159 (2012) F799–F803. doi:10.1149/2.016212jes.
[20] A.M. D'Angelo, A.C.Y. Liu, A.L. Chaffee, Oxygen Uptake of Tb–CeO2: Analysis of Ce3+ and Oxygen Vacancies, J. Phys. Chem. C. 120 (2016) 14382–14389. doi:10.1021/acs.jpcc.6b04063.
[21] G. Kresse, J. Furthmüller, Efficiency of ab-initio total energy calculations for metals and semiconductors using a plane-wave basis set, Comput. Meter. Sci. 6 (1996) 15–50. doi:10.1016/0927-0256(96)00008-0.
[22] G. Kresse, J. Furthmüller, Efficient iterative schemes for ab initio total-energy calculations using a plane-wave basis set, Phys. Rev. B. 54 (1996) 11169–11186. doi:10.1103/PhysRevB.54.11169.
[23] G. Kresse, D. Joubert, From ultrasoft pseudopotentials to the projector augmented-wave method, Phys. Rev. B. 59 (1999) 1758–1775. doi:10.1103/PhysRevB.59.1758.
[24] J.P. Perdew, K. Burke, M. Ernzerhof, Generalized Gradient Approximation Made Simple, Phys. Rev. Lett. 77 (1996) 3865–3868. doi:10.1103/PhysRevLett.77.3865.
[25] S.L. Dudarev, D.N. Manh, A.P. Sutton, Effect of Mott-Hubbard correlations on the electronic structure and structural stability of uranium dioxide, Phil. Mag. B. 75 (1997) 613–628. doi:10.1080/13642819708202343.
[26] P.R.L. Keating, D.O. Scanlon, B.J. Morgan, N.M. Galea, G.W. Watson, Analysis of Intrinsic Defects in CeO2 Using a Koopmans-Like GGA+U Approach, J. Phys. Chem. C. 116 (2012) 2443–2452. doi:10.1021/jp2080034.
[27] L. Shi, E. Vathonne, V. Oison, M. Freyss, R. Hayn, First-principles DFT+U investigation of charged states of defects and fission gas atoms in ${\mathrm{CeO}}_{2}$, Phys. Rev. B. 94 (2016) 115132. doi:10.1103/PhysRevB.94.115132.
[28] M.B. Kanoun, A.H. Reshak, N. Kanoun-Bouayed, S. Goumri-Said, Evidence of Coulomb correction and spin–orbit coupling in rare-earth dioxides CeO2, PrO2 and TbO2: An ab initio study, J. Mag. Mag. Mater. 324 (2012) 1397–1405. doi:10.1016/j.jmmm.2011.11.050.
[29] W. Tang, E. Sanville, G. Henkelman, A grid-based Bader analysis algorithm without lattice bias, J. Phys.: Condens. Matter. 21 (2009) 084204. doi:10.1088/0953-8984/21/8/084204.
[30] M. Yu, D.R. Trinkle, Accurate and efficient algorithm for Bader charge integration, J. Chem. Phys. 134 (2011) 064111. doi:10.1063/1.3553716.
[31] P. Villars, F. Hulliger, TbO2 valence/charge transfer: Datasheet from "PAULING FILE Multinaries Edition – 2012" in SpringerMaterials (https://materials.springer.com/isp/physical-property/docs/ppp_140103), Springer-Verlag Berlin Heidelberg & Material Phases Data System (MPDS), Switzerland & National Institute for Materials Science (NIMS), Japan, n.d. https://materials.springer.com/isp/physical-property/docs/ppp_140103.
[32] F. Ahmadpour, Y. Mozharivskyj, Structure of new metastable cubic TbO2−x, J. Alloys Compd. 452 (2008) 254–257. doi:10.1016/j.jallcom.2006.11.018.
[33] L. Gerward, J. Staun Olsen, L. Petit, G. Vaitheeswaran, V. Kanchana, A. Svane, Bulk modulus of CeO2 and PrO2—An experimental and theoretical study, J. Alloys Compd. 400 (2005) 56–61. doi:10.1016/j.jallcom.2005.04.008.
[34] L.-G. Liu, High-pressure phase transformations of fluorite-type dioxides, Earth Planet. Sci. Lett. 49 (1980) 166–172. doi:10.1016/0012-821X(80)90158-2.
[35] E. Wuilloud, B. Delley, W.-D. Schneider, Y. Baer, Spectroscopic Evidence for Localized and Extended f-Symmetry States in Ce${\mathrm{O}}_{2}$, Phys. Rev. Lett. 53 (1984) 202–205. doi:10.1103/PhysRevLett.53.202.
[36] D.D. Fontaine, Cluster Approach to Order-Disorder Transformations in Alloys, in: H. EHRENREICH, D. TURNBULL (Eds.), Solid State Physics, Academic Press, 1994: pp. 33–176. doi:10.1016/S0081-1947(08)60639-6.
[37] F. Ducastelle, Order and phase stability in alloys, North-Holland ; Sole distributors for the USA and Canada, Elsevier Science Pub. Co., Amsterdam; New York; New York, NY, USA, 1991.
[38] A. Zunger, First-Principles Statistical Mechanics of Semiconductor Alloys and Intermetallic Compounds, in: P.E.A. Turchi, A. Gonis (Eds.), Statics and Dynamics of Alloy Phase Transformations, Springer US, Boston, MA, 1994: pp. 361–419. doi:10.1007/978-1-4615-2476-2_23.
[39] J.W.D. Connolly, A.R. Williams, Density-functional theory applied to phase transformations in transition-metal alloys, Phys. Rev. B. 27 (1983) 5169–5172. doi:10.1103/PhysRevB.27.5169.
[40] A.V. Ruban, I.A. Abrikosov, D.Y. Kats, D. Gorelikov, K.W. Jacobsen, H.L. Skriver, Self-consistent electronic structure and segregation profiles of the Cu-Ni (001) random-alloy surface, Phys. Rev. B. 49 (1994) 11383–11396. doi:10.1103/PhysRevB.49.11383.

[41] C.R. Sax, B. Schönfeld, A.V. Ruban, Interactions and phase transformations in Fe-Pd, Phys. Rev. B. 89 (2014) 014201. doi:10.1103/PhysRevB.89.014201.
[42] A.G. Khachaturyan, Theory of structural transformations in solids, John Wiley & Sons, New York, 1983.
[43] D. Fuks, S. Dorfman, E.A. Kotomin, Y.F. Zhukovskii, A. Marshall Stoneham, Theoretical Analysis of the Growth Mode for Thin Metallic Films on Oxide Substrates, Phys. Rev. Lett. 85 (2000) 4333–4336. doi:10.1103/PhysRevLett.85.4333.
[44] D. Fuks, S. Dorfman, Y.F. Zhukovskii, E.A. Kotomin, A. Marshall Stoneham, Theory of the growth mode for a thin metallic film on an insulating substrate, Surf. Sci. 499 (2002) 24–40. doi:10.1016/S0039-6028(01)01692-2.
[45] D. Fuks, E.A. Kotomin, Y.F. Zhukovskii, A.M. Stoneham, Size and shape of three-dimensional Cu clusters on a $\mathrm{MgO}(001)$ substrate: Combined ab initio and thermodynamic approach, Phys. Rev. B. 74 (2006) 115418. doi:10.1103/PhysRevB.74.115418.
[46] Y.F. Zhukovskii, D. Fuks, E.A. Kotomin, D.E. Ellis, Differences in the metallic film growth mode between perfect and defective MgO surfaces, Nucl. Instrum. Methods Phys. Res., Sect. B. 255 (2007) 219–222. doi:10.1016/j.nimb.2006.11.025.
[47] D. Fuks, S. Dorfman, S. Piskunov, E.A. Kotomin, Ab initio thermodynamics of ${\mathrm{Ba}}_{\mathrm{c}}{\mathrm{Sr}}_{(1\ensuremath{-}\mathrm{c})}\mathrm{Ti}{\mathrm{O}}_{3}$ solid solutions, Phys. Rev. B. 71 (2005) 014111. doi:10.1103/PhysRevB.71.014111.
[48] D. Fuks, L. Bakaleinikov, E.A. Kotomin, J. Felsteiner, A. Gordon, R.A. Evarestov, D. Gryaznov, J. Maier, Thermodynamic stability and disordering in LacSr1−cMnO3 solid solutions, Solid State Ion. 177 (2006) 217–222. doi:10.1016/j.ssi.2005.10.014.
[49] A. Weizman, D. Fuks, E.A. Kotomin, D. Gryaznov, Ab initio study of phase competition in (La1−c,Src)CoO3 solid solutions, Solid State Ion. 230 (2013) 32–36. doi:10.1016/j.ssi.2012.09.007.
[50] D. Fuks, Weizman Amir, E.A. Kotomin, Phase competition in (La1 − c,Src)CoO3 solid solutions: ab initio thermodynamic study, Phys. Status Solidi B. 250 (2013) 864–869. doi:10.1002/pssb.201200851.
[51] K. Kirievsky, Y. Gelbstein, D. Fuks, Phase separation and antisite defects in the thermoelectric TiNiSn half-Heusler alloys, J. Solid State Chem. 203 (2013) 247–254. doi:10.1016/j.jssc.2013.04.032.
[52] G. Komisarchik, Y. Gelbstein, D. Fuks, Combined electronic and thermodynamic approaches for enhancing the thermoelectric properties of Ti-doped PbTe, Phys. Chem. Chem. Phys. 18 (2016) 32429–32437. doi:10.1039/C6CP06364K.
[53] M. Kaller, D. Fuks, Y. Gelbstein, Sc solubility in p-type half-Heusler (Ti1-cScc)NiSn thermoelectric alloys, J. Alloys Compd. 729 (2017) 446–452. doi:10.1016/j.jallcom.2017.09.137.
[54] E.M. Lifshitz, On the theory of phase transitions of the second order I., J. Phys. (USSR). VI (1942) 61–74.
[55] E.M. Lifshitz, On the theory of phase transitions of the second order II., J. Phys. (USSR). VI (1942) 251–263.
[56] L. Kaufman, H. Bernstein, Computer Calculation of Phase Diagrams: With Special Reference to Refractory Metals, Academic Press Inc, New York, 1970.
[57] P. Villars, F. Hulliger, Ce-O Binary Phase Diagram 63.5-67 at.% O: Datasheet from “PAULING FILE in: Inorganic Solid Phases” in SpringerMaterials (https://materials.springer.com/isp/phase-diagram/docs/c_0905169), Springer-Verlag Berlin Heidelberg & Material Phases Data System (MPDS), Switzerland & National Institute for Materials Science (NIMS), Japan, n.d. https://materials.springer.com/isp/phase-diagram/docs/c_0905169.
[58] P. Villars, F. Hulliger, O-Tb Binary Phase Diagram 34.7-40 at.% Tb: Datasheet from “PAULING FILE in: Inorganic Solid Phases” in SpringerMaterials (https://materials.springer.com/isp/phase-diagram/docs/c_0103549), Springer-Verlag Berlin Heidelberg & Material Phases Data System (MPDS), Switzerland & National Institute for Materials Science (NIMS), Japan, n.d. https://materials.springer.com/isp/phase-diagram/docs/c_0103549.
[59] R. Kikuchi, Superposition approximation and natural iteration calculation in cluster-variation method, J. Chem. Phys. 60 (1974) 1071–1080. doi:10.1063/1.1681115.
[60] T. Mohri, Y. Chen, N. Kiyokane, First-principles cluster variation calculations of tetragonal-cubic transition in ZrO2, J. Alloys Compd. 577 (2013) S123–S126. doi:10.1016/j.jallcom.2012.04.059.
[61] D.W. Hoffman, Configurational entropy and solute correlation in disordered alloys, Metallurgical Transactions. 3 (1972) 3231–3238. doi:10.1007/BF02661338.

[62] D. Fuks, Y. Mastrikov, E. Kotomin, J. Maier, Ab initio thermodynamic study of (Ba,Sr)(Co,Fe)O3 perovskite solid solutions for fuel cell applications, J. Mater. Chem. A. 1 (2013) 14320–14328. doi:10.1039/C3TA12874A.

Institute of Solid State Physics, University of Latvia as the Center of Excellence has received funding from the European Union's Horizon 2020 Framework Programme H2020-WIDESPREAD-01-2016-2017-TeamingPhase2 under grant agreement No. 739508, project CAMART²